Icarus 391 (2023) 115300

Contents lists available at ScienceDirect

Icarus

journal homepage: www.elsevier.com/locate/icarus

Water-rich C-type asteroids as early solar system carbonate factories

Victoria Froh [a], Maitrayee Bose [a,*], Martin D. Suttle [b,c], Jacopo Nava [d], Luigi Folco [b,e], Lynda B. Williams [a], Julie Castillo-Rogez [f]

[a] School of Earth and Space Exploration, Arizona State University, Tempe, AZ 85287, USA
[b] School of Physical Sciences, The Open University, Walton Hall, Milton Keynes MK7 6AA, UK
[c] Dipartimento di Scienze della Terra, Università di Pisa, 56126 Pisa, Italy
[d] University of Padova, Department of Geosciences, Via G.Gradenigo 6, 35131 Padova, Italy
[e] CISUP, Centro per l'Integrazione della Strumentazione dell'Università di Pisa, Lungarno Pacinotti 43, 56126 Pisa, Italy
[f] Jet Propulsion Laboratory, California Institute of Technology, 4800 Oak Grove Drive, Pasadena, CA 91109, USA

ARTICLE INFO

Keywords:
Micrometeorites
Meteorites
Carbonates
NanoSIMS
Isotopes
Asteroids

ABSTRACT

Micrometeorites represent a major potential source of volatiles for the early Earth, although often overlooked due to their small sizes and the effects of atmospheric entry. In this study we explore an unusual ~2000 μm, fine-grained unmelted micrometeorite TAM19B-7 derived from a water-rich C-type asteroid. Previous analysis revealed a unique O-isotope composition and intensely aqueously altered geological history. We investigated its carbon isotopic composition using the NanoSIMS and characterized the carbon-bearing carriers using Raman and Near-Infrared spectroscopy. We found that TAM19B-7 has a ^{13}C enriched bulk composition ($\delta^{13}C = +3 \pm 8$ ‰), including a domain with ^{13}C depletion ($\delta^{13}C = -27.1$ ‰). Furthermore, a few micro-scale domains show ^{13}C enrichments ($\delta^{13}C$ from +12.9 ‰ to +32.7 ‰) suggesting much of the particle's carbon content was reprocessed into fine-grained carbonates, likely calcite. The heavy bulk C-isotope composition of TAM19B-7 indicates either open system gas loss during aqueous alteration or carbonate formation from isotopically heavy soluble organics. Carbonates have been detected on small body surfaces, including across dwarf planet Ceres, and on the C-type asteroids Bennu and Ryugu. The preservation of both carbonates with ^{13}C enrichments and organic carbon with ^{13}C depletion in TAM19B-7, despite having been flash heated to high temperatures (<1000 °C), demonstrates the importance of cosmic dust as a volatile reservoir.

1. Introduction

Micrometeorites are cosmic dust particles on the micron – to – millimeter scale that originate from extraterrestrial bodies, pass through Earth's atmosphere, survive, and accumulate on the Earth's surface, where they can be collected for laboratory analyses (e.g., Kurat et al., 1994; Genge et al., 2008; Folco and Cordier, 2015). The TAM65 trap from where the sample in this study was recovered has a global annual flux estimate of 1555 (±753) tons/year (Suttle and Folco, 2020), consistent with previous micrometeorite abundance estimates from the South Pole Water Well estimate (~1600 tons/year: Taylor et al., 1998). Although meteorites can account for a larger mass, much of that material is often unrecoverable, having landed in remote areas or/and disintegrating during transit through the atmosphere or on Earth's surface (e.g., Dudorov and Eretnova, 2020). Micrometeorites, owing to their unique transport mechanisms in interplanetary space (Zook and Berg, 1975; Gonczi et al., 1982), sample a potentially much wider range of parent bodies than larger meteoroids, which implies that they allow exploration of an otherwise hidden diversity in the asteroid belt (Genge et al., 1997, 2008; Gounelle et al., 2009; Cordier et al., 2018). Thus, micrometeorites are a valuable resource for investigating the small-body population in the main belt of our solar system, providing a complementary perspective on the flux of extraterrestrial material to the Earth's surface.

Micrometeorites can be categorized into different classes based on their physical and mineralogical properties, and on their chemical and isotopic compositions (Genge et al., 2008; Folco and Cordier, 2015). At small size fractions (<500 μm) roughly 60–75% of particles originate from primitive and variably hydrated bodies (Taylor et al., 2012; Cordier and Folco, 2014), either C-type asteroids (Kurat et al., 1994; Genge, 2007; Genge et al., 2017) or comets (Engrand and Maurette, 1998; Dobrică et al., 2009; Noguchi et al., 2015). The remaining material

* Corresponding author.
E-mail address: Maitrayee.Bose@asu.edu (M. Bose).

https://doi.org/10.1016/j.icarus.2022.115300
Received 6 June 2022; Received in revised form 5 September 2022; Accepted 3 October 2022
Available online 12 October 2022

samples ordinary chondrite parent bodies while <1% of particles originate from differentiated achondritic bodies (Genge, 2008; Taylor et al., 2012; Cordier and Folco, 2014; Soens et al., 2022). By contrast, at larger size fractions (>500 μm) the cosmic dust flux is increasingly composed of ordinary chondrite material (Van Ginneken et al., 2012; Cordier and Folco, 2014).

Several studies have also reported hydrated fine-grained micrometeorites whose properties are inconsistent with known meteorite groups. For example, Battandier et al. (2018) reported higher CH_2/CH_3 ratios in a population of fine-grained micrometeorites and smaller carbonyl abundances relative to chondrites, which are features that are not attributable to atmospheric entry heating. Suttle et al. (2019a) described intensely aqueously altered particles containing low abundances of small chondrule (<200 μm) pseudomorphs. Their characteristics are also inconsistent with the CM, CR or CI chondrites. Perhaps the most prominent example of anomalous micrometeorites is the population of ^{16}O-poor micrometeorites (approximately δ^{17}O: 23.9‰, δ^{18}O: 42.0‰, Δ^{17}O: 2.0‰) first reported by Suavet et al. (2010) and termed "Group 4" spherules. The existence of the anomalous Group 4 spherules has since been confirmed by multiple independent studies (Van Ginneken et al., 2017; Suttle et al., 2020; Rudraswami et al., 2020). Typically, ^{16}O-rich compositions (that plot below the terrestrial fractionation line) are associated with carbonaceous chondrites, while ^{16}O-poor compositions (that plot above the terrestrial fractionation line) are associated with non-carbonaceous bodies. However, Suttle et al. (2020) demonstrated that the ^{16}O-poor "Group 4" micrometeorites originate from a hydrated carbonaceous parent body.

The presence of carbonaceous matter in extraterrestrial materials makes them a possible source for the delivery of biogenic molecules to Earth, potentially aiding in the development of life (Maurette, 1996; Dobrică et al., 2009). The average estimate of the amount of carbon delivered to Earth in present day by micrometeorites is over 50,000 times higher than meteorites, proving them to potentially be the major contributor to Earth's carbon (Maurette, 1996). This makes studying micrometeorites and the forms of carbon within them an important component of any astrobiology or geochemical modelling of the early Earth. However, the carbon isotopic composition and its abundance in micrometeorites remains poorly constrained. In this work, we explore these in a large hydrated fine-grained micrometeorite TAM19B-7, providing insights into the carbon cycle and budget on C-type asteroids, and the survivability of carbon-bearing materials in micrometeorites during atmospheric entry.

2. Sample: TAM19B-7

2.1. Particle provenance and analysis history

The micrometeorite TAM19B-7 was collected from a sedimentary trap on the summit of Miller Butte in the Transantarctic Mountains (TAM) in 2006 by the Italian Programma Nazionale di Ricerche in Antartide (PNRA) expeditions. These rock traps were exposed for a long duration of at least ~1 million years, as determined by the Ar—Ar ages of microtektites found in these traps (Folco et al., 2009; Di Vincenzo et al., 2021) and by the presence of micrometeorites recording reversed polarity found at this site (Suavet et al., 2011). The particles in the TAM collection include the full-size range of micrometeorites but is noteworthy for its large proportion of micrometeorites >400 μm (Rochette et al., 2008; Suavet et al., 2009; Suttle and Folco, 2020). TAM19B-7 measured roughly 2000 μm in diameter, when discovered.

TAM19B-7 was picked under the microscope after sieving from the host terrestrial sediment. It was embedded in resin, sectioned, polished, and analyzed with a scanning electron microscope (SEM) for back scattered electron (BSE) imaging and energy dispersive spectrometry (EDS), followed by analysis with an electron probe micro analyzer (EMPA), and elemental X-ray mapping, primarily at the National History Museum, London (Suttle et al., 2019a, 2019b). TAM19B-7 was then mechanically extracted from its epoxy resin mount and broken into smaller fragments. The main mass was destructively analyzed by infrared laser-assisted fluorination mass spectrometry at Open University in Milton Keyes, UK providing bulk O-isotope data (Suttle et al., 2020), while the remaining material (11 fragments) were re-embedded for higher-resolution BSE and EDS mapping on their newly exposed surfaces (Suttle et al., 2019a, 2019b). Finally, carbon isotopes were measured with the NanoSIMS 50L at Arizona State University on the mount containing the 11 fragments.

2.2. Terrestrial weathering

Like many of the extraterrestrial materials recovered from Antarctica, TAM19B-7 has suffered terrestrial alteration (weathering) during its residence on Earth. The sub-aerial micrometeorite traps at Miller Butte are a dry, oxidizing and mildly acidic environment (Van Ginneken et al., 2016). Micrometeorites within these traps were occasionally exposed to Antarctic water (Suttle et al., 2020). The main weathering features identified in TAM micrometeorites are etching and dissolution of silicate glass and anhydrous silicates, the oxidation of FeNi-metal and the infilling of voids by secondary minerals (primarily calcite, jarosite and halite). Encrustation rims, formed from the same secondary minerals are also common (Van Ginneken et al., 2016). In TAM19B-7 there is no evidence for metal oxidation, glass etching or loss of anhydrous silicates, although these phases would not be expected given its high degree of parent body aqueous alteration. Instead, the main weathering features affecting TAM19B-7 are the widespread formation of jarosite, previously described in Suttle et al. (2019a, 2019b).

2.3. Petrographic properties

Despite the effects of atmospheric entry heating and subsequent terrestrial weathering, the parent body properties of the particle TAM19B-7 can be confidently resolved and have been studied in detail. TAM19B-7 is a fine-grained micrometeorite enclosed by a magnetite rim and a well-developed igneous rim composed of silicate glass with a vesicular texture. This is a diagnostic feature found on (almost) all unmelted micrometeorites and indicates moderate thermal processing during atmospheric entry (Genge et al., 2008). The particle's internal mineralogy is dominated by Fe-rich phyllosilicates (or their thermal decomposition products) with no surviving anhydrous silicates (Suttle et al., 2019a). As in most unmelted fine-grained micrometeorites the interior phyllosilicates in TAM19B-7 are not well-formed crystalline, hydrated phases but a mix of recrystallized annealed olivine and partially amorphized residual phyllosilicate (as dehydroxylates) (Genge et al., 2008; Suttle et al., 2017). Small (~140 μm) elongated pseudomorphic chondrules occur at low abundances, while the phyllosilicate matrix defines a weak pervasive petrofabric (Suttle et al., 2019a). Thus, the texture, mineralogy, and elemental composition link TAM19B-7 to the hydrated carbonaceous chondrite group.

TAM19B-7 possesses a unique O-isotope composition (δ^{17}O: 1.1‰, δ^{18}O: 1.1‰, Δ^{17}O: 0.5‰, Suttle et al., 2020). This value plots above the TFL but at low δ^{18}O values in the three-oxygen isotope space. By contrast, all other hydrated carbonaceous chondrite materials that plot above the TFL have significantly higher δ^{18}O values: the CIs have average δ^{18}O values of 16.3‰, the CYs average values of 21.4‰ and the "Group 4" micrometeorites average δ^{18}O values of 42.0‰. The unusual O-isotope composition of TAM19B-7 has been explained by the terrestrial weathering that affected this particle whilst it resided in Antarctica. Incomplete equilibration with isotopically light Antarctic waters led to lower δ^{18}O values. Reconstructing the pre-weathering composition of TAM19B-7 indicates a positive Δ^{17}O ratio and a larger δ^{18}O value consistent with the other isotopically heavy hydrated carbonaceous chondrite materials (Suttle et al., 2020). Given the heterogeneous nature of Antarctic weathering, alteration of the particle's elemental composition and mineralogy cannot be quantified, and the exact parent body

affinities remain ambiguous.

3. Methods

3.1. Near-Infrared (IR) spectroscopy

Reflectance near-IR spectra were acquired at the IAPS-INAF in Rome (Istituto di Astrofisica e Planetologia Spaziali — Istituto Nazionale di Astrofisica). The instrument used was a microscope Micro-IR Hyperion 2000 FTIR Vertex Bruker®. Spectra were acquired in the spectral range between 1.3 and 22 μm with an MCT detector. However, here we report the data in the range of interest between 2 μm and 4 μm. To calibrate spectral reflectance an Infragold (Labsphere®) was used. The spectral resolution is of 2 cm^{-1} and an aperture on the sample of 150 × 150 μm.

3.2. Raman spectroscopy

Raman spectral data were collected at Diamond Lightsource Synchrotron facility (Didcot, UK), in the offline spectroscopy and support lab (91). Raman spectroscopy was employed to investigate the presence and properties of potential insoluble organic matter (IOM) within TAM19B-7. Raman spectral analysis is sensitive to the presence of macromolecular organic matter; positive identification is confirmed by the presence of characteristic *diamond-like* and/or *graphite-like* excitation features (referred to as D and G bands and located at ~1580 cm^{-1} and ~1600 cm^{-1} respectively). Analysis of D and G band peak parameters reveals insights into the structure and chemical state of IOM in chondritic materials (e.g., Busemann et al., 2007; Chan et al., 2019).

We used a Renishaw inVia Raman Microscope fitted with a 473 nm (green) laser source. Radiation was focused through a microscope using a 50× objective lens. This provided a nominal spot size of 1 μm diameter. We employed low laser powers (at the sample surface ~0.35 mW), achieving adequate signal-to-noise results whilst avoiding measurement-induced photooxidation of the target organic matter during analysis (consistent with previous observations reported by Chan et al., 2019). Spectra were collected over the spectral range of 600–2000 cm^{-1} using a 20 s exposure time. Three accumulations were averaged at each spot location, giving a total analysis time of 60s per spot.

We analyzed fragments F1, F5, F7 and F10, collecting >10 spectra per fragment in randomly located regions across the exposed surface area. However, only fragments F5 and F10 produced Raman spectra with identifiable G and D band peaks. This indicates that IOM was either absent or at very low concentrations in the remaining fragments (F1 and F7).

Raman spectra were processed to extract peak parameter data using the free curve fitting software *Fityk*. The baseline was modelled with a cubic spline function fitted against the spectrum at five locations (750 cm^{-1}, 1000 cm^{-1}, 1250 cm^{-1}, 1750 cm^{-1} and 2000 cm^{-1}). We used a 2-band model (two Lorentzian profiles) automatically refined using a Levenberg–Marquardt fitting algorithm. Peak position, intensity and full width half maximum (FWHM) parameters were recorded for both D and G bands.

3.3. (a) NanoSIMS

We received the TAM19B-7 fragments mounted in a 1-in. epoxy resin. Reflected light images were taken using a Nikon ECLIPSE LV100ND Industrial Microscope, and then the sample was gold coated using the Hummer sputter coater to prepare for analysis with the NanoSIMS 50L instrument. The sample was mounted into the sample holder along with a cyanoacrylate standard, also known as Krazy Glue (Bose et al., 2014), which was used for calibrating the carbon isotope data.

Areas on 11 fragments were chosen for analysis with the NanoSIMS based on composition and the likelihood of preserving carbon-bearing material, five of which were ultimately measured. Using the BSE images and EDX spot analysis data from the different fragments, areas with higher phosphorus and lower sulfur concentrations were selected, as high-phosphorus areas are more likely to contain biogenic materials, and sulfide minerals can be avoided. Darker areas in the BSE images were also selected as a potential indicator of higher carbon concentrations. In general, areas of the fragments with larger grains were avoided as they often include refractory silicate minerals. Fine-grained areas are also more likely to be carbonaceous, as has been observed typically in meteorites. In the reflected light microscope images, several areas on a few fragments (F4, F7, F8, F9 and F10) appeared as brownish in coloration and differed starkly from the rest of the dark appearance of the fragments. These areas were avoided for measurements because they could have been a result of alteration. Finally, charging was an issue for some coarse-grained particles, so those areas were avoided.

A 16 keV Cs^+ primary ion beam of 5 pA (D1–3 diameter of 200 μm) was used for isotope analysis with the NanoSIMS in the spot mode, with a current of 20 pA to pre-sputter and remove the gold coat in the areas of interest and to implant cesium. A 10 × 10 μm^2 raster was used to pre-sputter, while a 5 × 5 μm^2 raster was used for isotopic analysis. Each raster frame is divided into 256 × 256 pixels, with each pixel having a dwell time of either 1000 or 1500 μs. For the standards, the total measurement time ranged between roughly 390 and 790 s, while the total time for the TAM19B-7 samples ranged between roughly 720 and 3600 s. Secondary ions of $^{12}C^-$, $^{13}C^-$, and $^{28}Si^-$ were measured simultaneously in multi-collection mode. The Cameca mass resolving power (MRP) was >8600 and the actual MRP calculated from the peak shapes is ~5400 with the entrance slit ES-3 (30x180μm^2) and the aperture slit AS-3 (150x150μm^2); this MRP is adequate to separate the isobaric interference of $^{12}C^1H$ from ^{13}C (required MRP is 2916). Several spots on five different fragments were measured, with the Krazy Glue standard measurements being done at regular intervals. The epoxy resin surrounding the particles was also measured to distinguish it from the porous domains within the particles. We also attempted to measure nitrogen but $^{12}C^{15}N^-$ counts were well below 100 counts per pixel for several particles, and hence are not reported here.

The raw data from measurements was statistically analyzed and any values outside of 2σ from the average value for that run were rejected. The dead-time corrected total count values, for each isotope of every measurement were used to calculate the $^{13}C/^{12}C$ and $^{12}C/^{28}Si$ ratios, where the dead time for electron multipliers on our NanoSIMS is 44 ns. In order to account for instrumental mass fractionation, which is any non-proportional partitioning of the heavy and light isotopes of an element caused by the instrument, the $^{13}C/^{12}C$ ratios were normalized to the terrestrial ratio value of 0.0112 using an alpha ratio where:

$$\alpha_{SIMS} = \left(^{13}C/^{12}C\right)_{SIMS} \Big/ \left(^{13}C/^{12}C\right)_{VPDB}$$

An average of the alpha ratios for the Krazy Glue standard, 0.95, was used as the normalization factor for the Krazy Glue, epoxy and TAM19B-7 $^{13}C/^{12}C$ ratio values. The $^{13}C/^{12}C$ ratio values were then used to calculate the $\delta^{13}C$ values of the epoxy and the TAM18B-7 fragments, where:

$$\delta^{13}C = 1000\left[\left(^{13}C/^{12}C\right)_{Sample} \Big/ \left(^{13}C/^{12}C\right)_{Standard} \right) -1\Big]$$

was calculated relative to the NIST standard VPDB ($^{13}C/^{12}C$ = 0.0112) and the internal reference standard Krazy Glue. The $\delta^{13}C$ is used as a signature to track the carbon isotopic composition and compare it to different samples and groups, and the normalization to the 0.0112 value allows for our values to be compared to other values normalized to the international standard VPDB (Gröning, 2004).

3.4. (b) 6f SIMS

To calculate the carbon contents of the measured domains, we measured the Krazy Glue as an internal reference along with two other

polymers namely Araldite 502 and Polyethylene terephthalate (PET) with known, homogeneous carbon contents of 0.714 wt.% and 0.626 wt. % (Teichert et al., 2022), respectively. Using a Cs^+ primary ion beam $^{12}C^-$ and $^{16}O^-$ were measured (current varying from 100 to 300 pA) on several spots within each of the samples, which were gold coated to alleviate charging. The smallest secondary ion beam field aperture was used to limit the analyzed area to an 8 μm (diameter) area on the samples, using a mass resolving power of about 3000 to separate $^{24}Mg^{2+}$ from $^{12}C^+$. Areas were pre-sputtered until the carbon signal was stable, and the total measurement time depended on the sample (for statistically significant results) but was generally <15 min on each spot. The total ^{12}C counts were kept constant at ~300 k to avoid flooding the electron multiplier detector. We used a two-point calibration on Araldite and PET polymer samples to calculate that the carbon content of the Krazy Glue to be 0.581 wt.%.

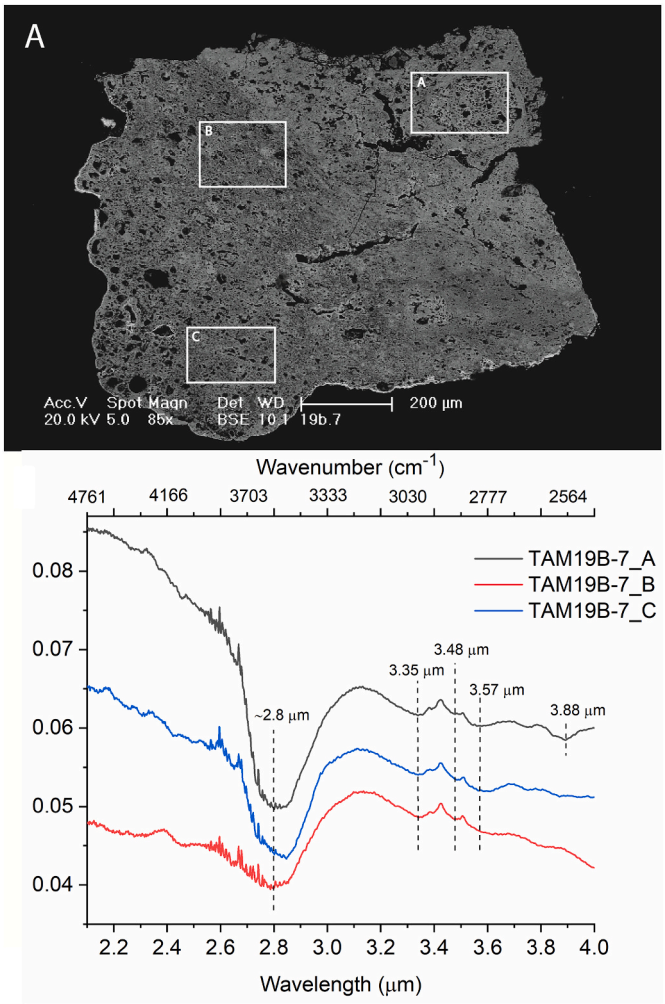

Fig. 1. A) BSE image of the TAM19B-7 micrometeorite (prior to fragmentation). Highlighted with white squares are the areas where we acquired the near-IR spectra. B) Reflectance spectra of the TAM19B-7 in the near-IR range. The observed absorption bands are the 2.8 μm band indicating hydrated minerals (i.e., phyllosilicates), the 3.3–3.6 μm range is related to the presence of alkanes, and the 3.9 μm band is due to the presence of carbonates. In the section view shown in A, the top and right-hand sides of TAM19B-7 have fractured faces indicating the original micrometeorite was bigger [Suttle et al., 2019a,b]

4. Results

4.1. IR spectroscopic data

Near-IR reflectance spectra of TAM19B-7 (Fig. 1) show a prominent 2.8 μm band (varying from 2.8 μm and 2.85 μm) indicative of hydrated Fe-rich phyllosilicates (Takir et al., 2013). In the 3.3–3.6 μm range, several absorption bands related to organic matter, in particular -CH functional groups indicative of alkanes were observed. The spectra acquired in an area also show a feature centered at 3.9 μm typical of carbonates (De Sanctis et al., 2016). Carbonates also contribute to the different features in the 3.3–3.6 μm range (Kaplan et al., 2020; Simon et al., 2020).

4.2. Raman data

Raman spectra of most regions in the TAM19B-7 particles do not produce signals containing D and G bands. They instead reveal noisy spectra with strong fluorescence backgrounds, which implies that IOM is either absent or occurs at very low concentrations throughout most of the micrometeorite, having been oxidized and destroyed during the particle's passage through Earth's atmosphere. However, multiple regions, occurring as isolated pockets in fragments F5 and F10, contained well-defined D and G bands. They always have similar profiles with a wider and lower intensity D band adjacent to a taller, thinner G band. Average ($N = 21$) peak parameters are D band position: 1375 (±4 [1σ]) cm^{-1}, FWHM: 141 (±25 [1σ]) cm^{-1} and G band position: 1595 (±3 [1σ]) cm^{-1}, FWHM: 116 (±35 [1σ]) cm^{-1}. The average ratio of peak intensities ($R_1 = D/G$) is 0.66.

4.3. Carbon isotope measurements

Five different fragments of TAM19B-7 were measured: 8 spots on fragment F1, 6 spots on F2, 1 spot on F7, 3 spots on F10, and 1 spot on F11 for a total of 19 different measurement spots (Fig. 2). The $^{13}C/^{12}C$ ratios, $\delta^{13}C$ values in permille (‰) and the $^{12}C/^{28}Si$ ratios are reported in Fig. 3, while the values for all individual sample and standard measurements are listed in Table 1. The $\delta^{13}C$ values for the Krazy Glue standard averaged 0 ± 12‰ (2σ), with 12 being the 2σ standard error with reference to the mean. For the epoxy resin, the $\delta^{13}C$ averaged −2 ± 6‰, which falls within the Krazy Glue range. As discussed below, several points on TAM19B-7 have $\delta^{13}C$ values that do not fall within the range noted for epoxy and are therefore provide carbon isotopic compositions of the micrometeorite.

Fifteen of the nineteen measured spots on TAM19B-7 are within the 2σ error range for the Krazy Glue standard while four carbon isotopically anomalous spots were identified (Fig. 3). The average $\delta^{13}C$ for the 15 spots is defined as the bulk value and was +3 ± 8‰ (Fig. 3). Three of the four anomalous spots were enriched in^{13}C and had $\delta^{13}C$ values of +12.9‰ (F1–200), +16.8‰ (F5–106), and + 32.7‰ (F10–101), while F1–207 was depleted in ^{13}C and had a $\delta^{13}C$ value of −27.1‰ (Fig. 3). Note that the measured isotopic anomalies are likely lower limits owing to some degree of isotopic dilution. The degree of isotopic dilution will vary with location (proximity to the epoxy) and porosity of the samples at that location and is impossible to quantify.

A majority of the measured spots had $^{12}C/^{28}Si$ ratios up to 6.5, except F1_200. Area F1_200 has an unusually high value C/Si ratio of ~3×10^4, 3 orders of magnitude above the bulk value and has a carbon content 0.93 wt%. F1_207 with a $^{12}C/^{28}Si$ ratio of 6.5 has a carbon content of ~2 ppm.

5. Discussion

5.1. Heating during atmospheric entry

Heating during atmospheric entry will affect the mineralogy and

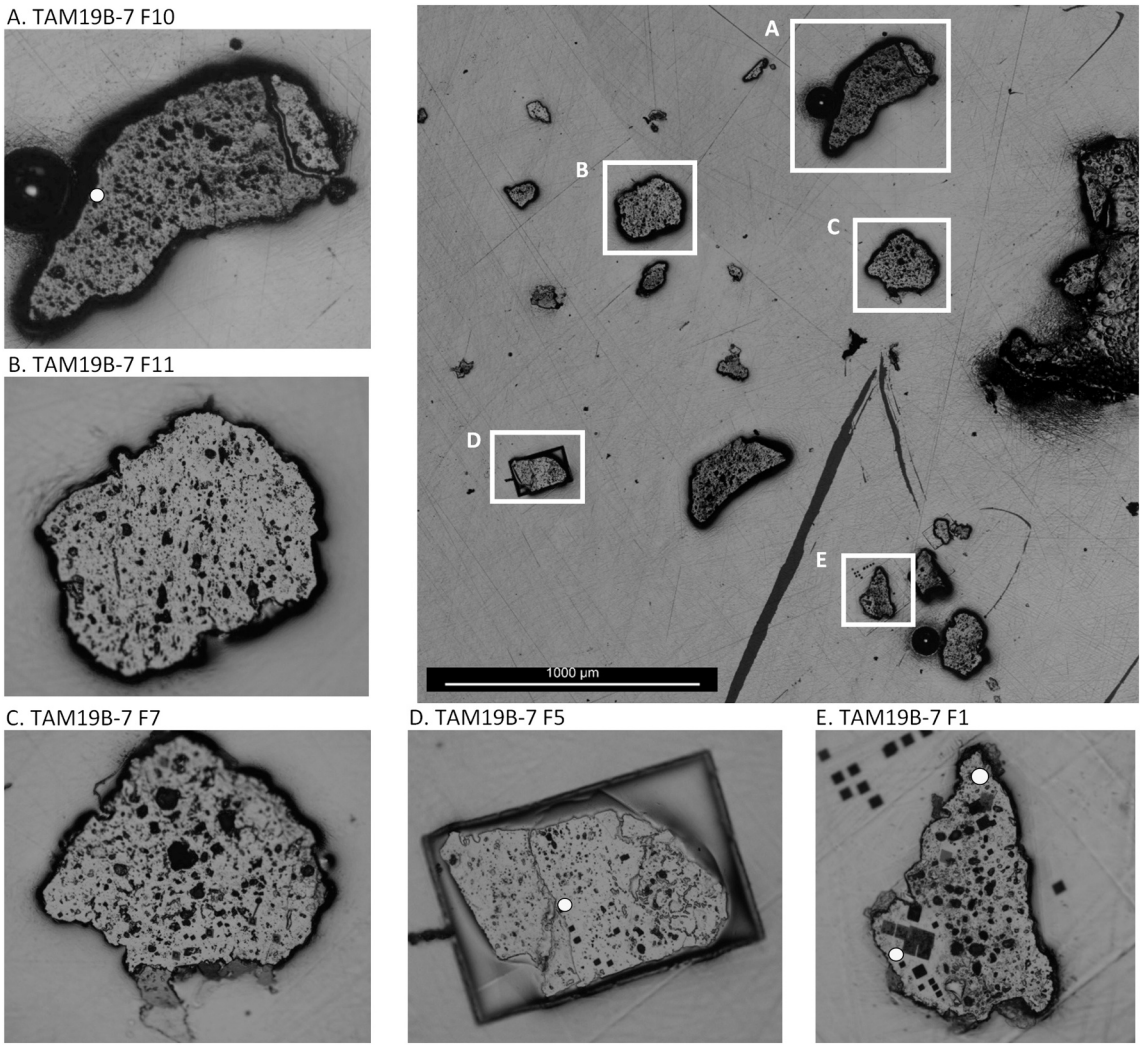

Fig. 2. Sample layout for the TAM19B-7 fragments. The 5 fragments (A-E) measured in the NanoSIMS are magnified and placed on the left and bottom. Excluding fragment F7, several areas on each fragment were measured for carbon isotopes. Examples of the measured areas can be seen as black boxes in E (fragment F1) in both the epoxy resin outside of the fragment and on the fragment. The small black boxes are the measured areas, compositions of which are discussed in this paper and measure 5×5 µm^2 on the fragment and 10×10 µm^2 in the epoxy. Grey dots indicate the locations of the four measured carbon-anomalous domains: F10–101, F5–106, F1–200 and F1–207. Fragments F5 and F10 produced Raman spectra with identifiable G and D band peaks.

carbon-bearing phases present in a micrometeorite, as well as their isotopic compositions. To understand what carbonaceous phases were present, prior to entry and how they may have been altered, or potentially destroyed, the maximum temperatures experienced during entry need to be examined. Pronounced thermal gradients form within cosmic dust during atmospheric entry, as evidenced by the presence of igneous rims on unmelted micrometeorites (Genge, 2006), the presence of thermally fractured anhydrous silicates near the margins of micrometeorites (Genge et al., 2017) and the observation of systematic changes in volatile element distribution (Toppani et al., 2001) and/or porosity (Dionnet et al., 2020) across individual particles.

TAM19B-7 has a well-developed igneous rim composed of silicate glass with a vesicular texture. These rims form by localized melting at the particle margin (Genge, 2006) and, therefore, attest to peak temperatures above the solidus of chondritic materials, approximately >1000 °C (Toppani et al., 2001). However, inwards of the rim, the core of the particle experienced lower temperatures as shown by the unmelted core which is instead dominated by phyllosilicate dehydration cracks.

Flash heating of phyllosilicates results in progressive dehydration, followed by loss of structural order and crystallinity (dehydroxylation), followed by recrystallization into a nanophase groundmass of anhydrous olivine. Phyllosilicates begin to dehydroxylate at ~400 °C, losing octahedral OH between 600 and 700 °C and form amorphous dehydroxylates and subsequently recrystallize to Fe-bearing olivine (Akai, 1992; Genge et al., 2008; Suttle et al., 2017) at 800–900 °C. The mid-IR spectra of TAM19B-7 reveals an amorphous smooth asymmetric peak centered at 9.2 µm and associated with Si—O bonds in a poorly crystalline silicate. These indicate the loss of absorbed and (most) structural water from phyllosilicates. However, the absence of an olivine spectral signature indicates that limited thermal annealing has occurred during entry, placing TAM19B-7 into the spectral group 2 category defined by Suttle et al. (2017), consistent with peak entry temperatures between 300 and 800 °C.

Peak temperatures in the core of TAM19B-7 can be further constrained by analysis of the near-IR spectra. These were collected from three regions within TAM19B-7 (Fig. 1). Sites A and B, sample regions close to the former center of the micrometeorite. They have deep, well-resolved 3-µm bands associated with M-OH bonds, indicating the survival of at least some hydrated phyllosilicate. By contrast, site C, located close to the igneous rim, has a shallower band, indicative of reduced water content. The near-IR spectra, therefore, reveal variations in the

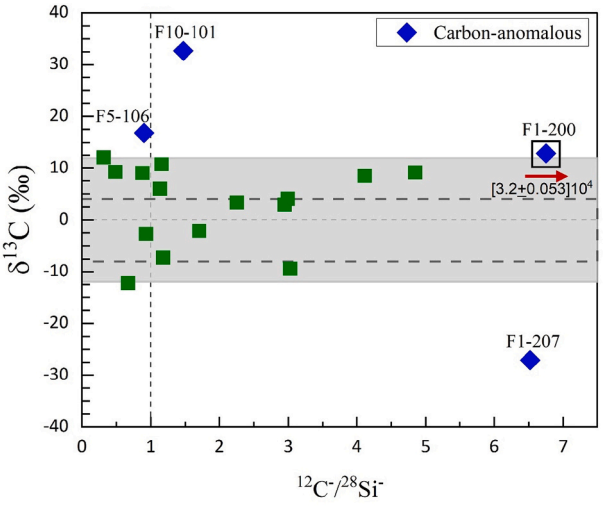

Fig. 3. $^{12}C^{-}/^{28}Si^{-}$ ratios vs $\delta^{13}C$ permille for the TAM19B-7 sample measurements. The grey box shows the range of the Krazy Glue average $\delta^{13}C \pm 2\sigma$, while the dark grey dotted lines show the range for the epoxy in which TAM19B-7 particles are embedded. Measurements (plotted as green squares) within these ranges were used to calculate the bulk $\delta^{13}C$ for TAM19B-7. The 2σ errors on the measurements are included but are smaller than the plotted symbols. Four measurements outside of this range are carbon-anomalous domains. The data point F1_200 within the black square has a $^{12}C^{-}/^{28}Si^{-}$ ratio that is 4 orders of magnitude higher than the remaining measurements. The dotted vertical line at $^{12}C^{-}/^{28}Si^{-} = 1$ represents the average value seen in presolar silicon carbide grains, above which indicates a particle being C-rich. (For interpretation of the references to colour in this figure legend, the reader is referred to the web version of this article.)

retention of M-OH bonds within the phyllosilicate matrix that appear to correlate with proximity to the particle margin. The retention of hydrated phyllosilicates is significant because this constrains peak temperatures in the interior to <800 °C (the decomposition temperature of saponite [Garenne et al., 2014]). Furthermore, the near-IR spectra provide tentative evidence for organics and carbonate minerals (features located at 3.3–3.6 μm and 3.9 μm). Carbonate minerals thermally decompose at temperatures between approximately 770–900 °C (Garenne et al., 2014).

The evolution of organic matter, as traced by changes in G and D bands (observed using Raman spectroscopy) provide additional insights into the peak temperature. The average peak parameters of TAM19B-7 (Fig. 4) are distinct from unheated chondritic materials (Busemann et al., 2007), which typically have D and G bands of approximately equal height combined with thinner G bands (FWHM: < 100 cm^{-1}) centered at lower Raman shift values (~1585 cm^{-1}) than those observed in TAM19B-7. Likewise, D bands are generally broader (FWHM: > 150 cm^{-1}) with band centers located at ~1350 cm^{-1} (Busemann et al., 2007). Conversely, the peak parameters calculated from Raman spectra taken on TAM19B-7 (Fig. 4) are consistent with previously reported fine-grained micrometeorites (Battandier et al., 2018). Thermal processing of IOM results in graphitization, observed in Raman spectra as a loss of disordered diamond-like bonds (resulting in a less pronounced D band) and growth in the intensity and width of the G band (Busemann et al., 2007). Comparisons with short-duration experimentally heated samples of Tagish Lake (Fig. 4) suggests peak temperatures >600 °C and < 900 °C (Chan et al., 2019). Furthermore, regions within TAM19B-7 where no D and G bands were detected using Raman spectral analysis (e.g., Fragments F1 and F7) imply peak temperatures >900 °C (i.e., definitely unmelted) thereby indicating that heating with TAM19B-7 was locally variable.

Table 1
Carbon isotopic composition and $^{12}C/^{28}Si$ ratio of TAM19B-7 fragments and standards.

Sample Name	$^{13}C/^{12}C$	$\delta^{13}C$	$^{12}C/^{28}Si$
Krazy Glue (KG) Standard			
KG_1	[1.14 ± 0.01] x 10^{-2}		[2.23 ± 0.04] x 10^{+4}
KG_2	[1.11 ± 0.01] x 10^{-2}		[1.47 ± 0.02] x 10^{+4}
KG_3	[1.12 ± 0.01] x 10^{-2}		[1.22 ± 0.03] x 10^{+4}
KG_4	[1.13 ± 0.01] x 10^{-2}		[1.45 ± 0.04] x 10^{+4}
KG_5	[1.13 ± 0.01] x 10^{-2}		[1.66 ± 0.04] x 10^{+4}
KG_6	[1.12 ± 0.01] x 10^{-2}		[1.43 ± 0.04] x 10^{+4}
KG_7	[1.12 ± 0.01] x 10^{-2}		[1.64 ± 0.04] x 10^{+4}
KG_8	[1.12 ± 0.01] x 10^{-2}		[1.86 ± 0.05] x 10^{+4}
KG_9	[1.11 ± 0.01] x 10^{-2}		[1.49 ± 0.04] x 10^{+4}
KG_10	[1.12 ± 0.01] x 10^{-2}		[1.66 ± 0.04] x 10^{+4}
KG_11	[1.12 ± 0.01] x 10^{-2}		[1.84 ± 0.05] x 10^{+4}
KG_12	[1.11 ± 0.01] x 10^{-2}		[1.27 ± 0.03] x 10^{+4}
KG_13	[1.11 ± 0.01] x 10^{-2}		[1.56 ± 0.04] x 10^{+4}
KG_14	[1.12 ± 0.01] x 10^{-2}		[1.79 ± 0.05] x 10^{+4}
KG_15	[1.11 ± 0.01] x 10^{-2}		[1.14 ± 0.03] x 10^{+4}
KG_16	[1.12 ± 0.01] x 10^{-2}		[1.46 ± 0.04] x 10^{+4}
KG_17	[1.12 ± 0.01] x 10^{-2}		[1.70 ± 0.04] x 10^{+4}
KG_18	[1.12 ± 0.01] x 10^{-2}		[1.12 ± 0.03] x 10^{+4}
KG_19	[1.12 ± 0.01] x 10^{-2}		[1.41 ± 0.04] x 10^{+4}
KG_20	[1.12 ± 0.01] x 10^{-2}		[1.67 ± 0.05] x 10^{+4}
KG_21	[1.11 ± 0.01] x 10^{-2}		[1.33 ± 0.03] x 10^{+4}
KG_22	[1.12 ± 0.01] x 10^{-2}		[1.58 ± 0.04] x 10^{+4}
KG_23	[1.12 ± 0.01] $^{x\ 10^{-2}}$		[1.79 ± 0.05] x 10^{+4}
KG_24	[1.13 ± 0.01] x 10^{-2}		[5.78 ± 0.30] x 10^{+4}
KG_25	[1.11 ± 0.01] x 10^{-2}		[4.60 ± 0.24] x 10^{+4}
KG_26	[1.12 ± 0.01] x 10^{-2}		[6.43 ± 0.34] x 10^{+4}
KG_27	[1.12 ± 0.01] x 10^{-2}		[2.53 ± 0.08] x 10^{+4}
KG_28	[1.13 ± 0.01] x 10^{-2}		[2.56 ± 0.08] x 10^{+4}
KG_29	[1.11 ± 0.01] x 10^{-2}		[1.69 ± 0.05] x 10^{+4}
KG_30	[1.12 ± 0.01] x 10^{-2}		[2.36 ± 0.07] x 10^{+4}
KG_31	[1.12 ± 0.01] x 10^{-2}		[2.62 ± 0.07] x 10^{+4}
KG_32	[1.12 ± 0.01] x 10^{-2}		[1.69 ± 0.05] x 10^{+4}
KG_33	[1.12 ± 0.01] x 10^{-2}		[2.35 ± 0.07] x 10^{+4}
KG_34	[1.13 ± 0.01] x 10^{-2}		[2.51 ± 0.07] x 10^{+4}
KG_35	[1.13 ± 0.01] x 10^{-2}		[2.18 ± 0.06] x 10^{+4}
KG_36	[1.13 ± 0.01] x 10^{-2}		[2.19 ± 0.07] x 10^{+4}

(continued on next page)

Table 1 (*continued*)

Sample Name	$^{13}C/^{12}C$	$\delta^{13}C$	$^{12}C/^{28}Si$
KG_37	[1.11 ± 0.01] x 10^{-2}		[1.25 ± 0.04] x 10^{+4}
KG_38	[1.11 ± 0.01] x 10^{-2}		[1.50 ± 0.06] x 10^{+4}
KG_39	[1.12 ± 0.01] x 10^{-2}		[1.93 ± 0.07] x 10^{+4}
KG_40	[1.11 ± 0.01] x 10^{-2}		[8.45 ± 0.02] x 10^{+3}
KG_41	[1.12 ± 0.01] x 10^{-2}		[1.28 ± 0.04] x 10^{+4}
KG_42	[1.12 ± 0.01] x 10^{-2}		[1.78 ± 0.07] x 10^{+4}
Average	1.12E-02	**0 ± 12**	2.00E+04
1 sigma	5.8	**5.8**	5.6E+02
Epoxy (Ep)			
Ep_1	[1.12 ± 0.01] x 10^{-2}	−3.8 ± 0.2	[1.37 ± 0.03] x 10^{+4}
Ep_2	[1.12 ± 0.01] x 10^{-2}	−3.7 ± 0.1	[1.43 ± 0.03] x 10^{+4}
Ep_3	[1.12 ± 0.01] x 10^{-2}	−4.0 ± 0.2	[1.45 ± 0.03] x 10^{+4}
Ep_4	[1.12 ± 0.01] x 10^{-2}	0.6 ± 0.0	[1.25 ± 0.02] x 10^{+4}
Ep_5	[1.12 ± 0.01] x 10^{-2}	0.9 ± 0.0	[1.35 ± 0.03] x 10^{+4}
Ep_6	[1.12 ± 0.01] x 10^{-2}	3.6 ± 0.1	[1.98 ± 0.05] x 10^{+4}
Ep_7	[1.12 ± 0.01] x 10^{-2}	0.8 ± 0.0	[1.39 ± 0.03] x 10^{+4}
Ep_8	[1.12 ± 0.01] x 10^{-2}	0.2 ± 0.0	[9.38 ± 0.87] x 10^{+4}
Ep_9	[1.11 ± 0.01] x 10^{-2}	−6.1 ± 0.2	[3.16 ± 0.74] x 10^{+5}
Ep_10	[1.12 ± 0.01] x 10^{-2}	−2.6 ± 0.1	[1.43 ± 0.03] x 10^{+4}
Ep_11	[1.12 ± 0.01] x 10^{-2}	−2.8 ± 0.1	[1.45 ± 0.03] x 10^{+4}
Ep_12	[1.12 ± 0.01] x 10^{-2}	−1.1 ± 0.0	[1.48 ± 0.03] x 10^{+4}
Average		**−1.5 ± 5.6**	
1 sigma		**2.8**	
TAM19B-7			
F1_200	[1.13 ± 0.01] x 10^{-2}	12.9 ± 0.5	[3.19 ± 0.11] x 10^{+4}
F1_202	[1.12 ± 0.01] x 10^{-2}	3.3 ± 0.1	2.25 ± < 0.01
F1_203	[1.12 ± 0.01] x 10^{-2}	2.9 ± 0.1	2.95 ± < 0.01
F1_204	[1.13 ± 0.01] x 10^{-2}	8.5 ± 0.3	4.12 ± < 0.01
F1_205	[1.12 ± 0.01] x 10^{-2}	4.1 ± 0.2	2.99 ± < 0.01
F1_206	[1.13 ± 0.01] x 10^{-2}	9.2 ± 0.4	4.84 ± < 0.01
F1_207	[1.09 ± 0.01] x 10^{-2}	−27.1 ± 1.1	6.52 ± 0.01
F1_208	[1.11 ± 0.01] x 10^{-2}	−9.4 ± 0.4	3.03 ± < 0.01
F5_101	[1.12 ± 0.02] x 10^{-2}	−2.7 ± 0.1	[9.27 ± 0.01] x 10^{-1}
F5_102	[1.13 ± 0.02] x 10^{-2}	6.0 ± 0.3	1.13 ± < 0.01
F5_103	[1.13 ± 0.02] x 10^{-2}	9.1 ± 0.4	[8.76 ± 0.01] x 10^{-1}
F5_104	[1.13 ± 0.02] x 10^{-2}	9.3 ± 0.4	[4.86 ± 0.01] x 10^{-1}
F5_105	[1.13 ± 0.02] x 10^{-2}	12.1 ± 0.6	[3.16 ± 0.02] x 10^{-1}
F5_106	[1.14 ± 0.02] x 10^{-2}	16.8 ± 0.7	[9.01 ± 0.04] x 10^{-1}
F7_200	[1.11 ± 0.02] x 10^{-2}	−12.3 ± 0.6	[6.70 ± 0.03] x 10^{-1}

Table 1 (*continued*)

Sample Name	$^{13}C/^{12}C$	$\delta^{13}C$	$^{12}C/^{28}Si$
F10_100	[1.12 ± 0.02] x 10^{-2}	−2.1 ± 0.1	1.70 ± < 0.01
F10_101	[1.16 ± 0.01] x 10^{-2}	32.7 ± 1.4	1.47 ± 0.01
F10_102	[1.13 ± 0.02] x 10^{-2}	10.7 ± 0.5	1.16 ± 0.01
F11_100	[1.11 ± 0.01] x 10^{-2}	−7.3 ± 0.3	1.18 ± < 0.01
Average (all points)		**4.0± 12.7**	

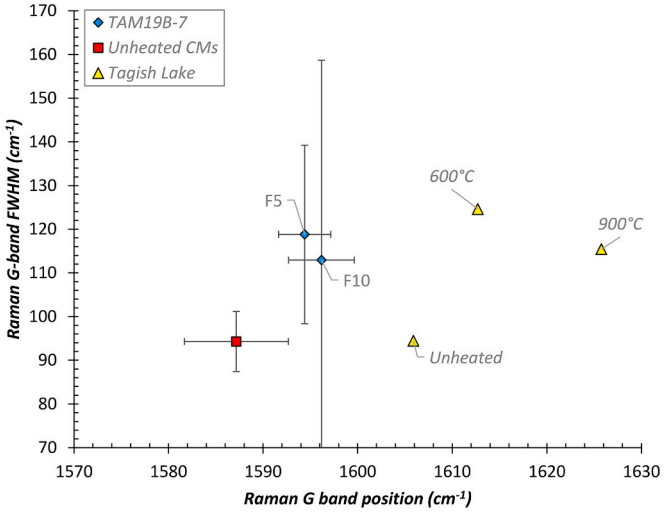

Fig. 4. Raman spectral data (peak parameters: G-band position and FWHM) collected on fragments F5 and F10 of micrometeorite TAM19B-7 compared against published data from insoluble organic matter extracted from unheated CMs (Busemann et al., 2007) and heated Tagish Lake meteorite matrix (Chan et al., 2019). These data imply peak temperatures in some regions of the TAM19B-7 sample to be low, and highly heterogenous.

5.2. Mineralogy and chemistry of the parent asteroid body

When a parent body experiences aqueous alteration, the primary lithology is slowly replaced with secondary minerals as the original anhydrous mafic silicates, such as olivine and pyroxene, react with the fluid phase. As alteration progresses, the anhydrous crystals lose Mg from dissolution, and most often reprecipitate as secondary Mg-rich and Fe-rich phyllosilicates and sometimes carbonates. With progressive alteration, the primary accretionary texture recrystallizes likely into Mg-rich phases that are stable under the new T, P conditions (Howard et al., 2015). When the fluid is consumed, the precipitation of phyllosilicates stops, and relict minerals of anhydrous silicate crystals may remain. As a result, chondrules or other refractory phases may be replaced with secondary phyllosilicates. Because aqueous alteration results in progressively more phyllosilicates and fewer anhydrous silicates, the phyllosilicate fraction is sometimes used to roughly determine the degree of alteration (Howard et al., 2015) and is calculated by:

$$\frac{\textit{total mass of phyllosilicates}}{\textit{total mass of phyllosilicates} + \textit{total mass of anhydrous silicates}}$$

TAM19B-7 had a pre-entry phyllosilicate fraction of 0.97, meaning that 97% of the micrometeorite mass was composed of phyllosilicates. This is on the extreme end of the range typically seen in hydrated carbonaceous chondrites, as CR's typically range 2.8–1.3 and CM's 1.7–1.2, where the lowest phyllosilicate fraction is 3.0 and the highest fraction is 1.0 (Howard et al., 2015). A fraction of 0.97 shows intense aqueous alteration and correlates to a petrologic subtype <1.1, which

indicates it comes from a completely hydrated parent body (Suttle et al., 2019a). Note that such a high pre-entry phyllosilicate fraction has been calculated for a < 2 mm-sized particles and may not be representative of meteorite-scale rocks and definitely not of its parent body.

5.3. Bulk Carbon-isotope composition

Bulk $\delta^{13}C$ in carbonaceous chondrites ranges from −19.9 to +3.7‰, in ordinary chondrites is from −25.9 to +6.4‰ and in enstatite chondrites from −14.1 to −4.1‰ (Alexander et al., 2012; Grady et al., 1988). Data from interplanetary dust particles (IDPs) which are the smallest subset of cosmic dust grains (<50 μm) has also been reported and reveals significant variation (from −70 to +10‰ over the light range plus some anomalous grains with an unusually heavy or light compositions (Fig. 5). IDPs likely sample both asteroids and comets. By comparison our calculated bulk $\delta^{13}C$ composition for TAM19B-7 (+3 ± 8‰; 2σ) has an enriched (heavy) value relative to most other extraterrestrial materials (Fig. 5). This bulk overlaps with the heavy end of the carbonaceous chondrite field (whilst being distinct from the ordinary and enstatite chondrites). However, the closest similarity is with the ungrouped carbonaceous chondrite Tagish Lake (from +9.4 to +14‰, Alexander et al., 2012). This implies both materials may have had a similar carbon chemistry.

Bulk compositions are an average of individual components. In chondrites there are three main carbon-bearing components: organic matter, carbonates and presolar grains (e.g., SiC, presolar nanodiamonds and interstellar graphite). Because TAM19B-7 experienced advanced aqueous alteration, the survival of presolar grains is unlikely (Floss et al., 2010; Floss and Stadermann, 2009; Bose et al., 2014). This leaves a mix of organic matter and carbonates as the dominant carbon-bearing materials.

The primitive accretionary assemblage of carbonaceous chondrite parent bodies would have included a mix of carbon-bearing ices (e.g., CO, CO_2 and CH_4 ices which are predicted to have had isotopically heavy $\delta^{13}C$ values, as supported by measurements of CO_2 ice from comet 67P/Churyumov–Gerasimenko (+65‰ ±51‰, Hässig et al., 2017) and primitive organic matter inherited either from the protoplanetary disk or the interstellar medium (e.g., Bose et al., 2012, 2014). This organic matter included both soluble short-chain molecules and larger acid-insoluble polyaromatic macromolecules. These two components have different $\delta^{13}C$ values (Fig. 5). Insoluble organic matter (IOM) has isotopically light compositions, ranging from $\delta^{13}C$: −34.2 to −4.5‰ (Alexander et al., 2007, 2010; Fig. 5), while soluble organic matter (SOM) has isotopically variable compositions which extend to heavy values ($\delta^{13}C$: −15 to +60‰, Sephton, 2002; Gilmour, 2014; Aponte et al., 2016). Residual, impact and radiogenic heating on early formed chondritic planetesimals melted ices and drove aqueous alteration reactions. This led to the generation of secondary carbonate minerals, primarily calcite (Grady et al., 1988; Alexander et al., 2015; Kaplan et al., 2020). As aqueous alteration advanced, organic matter was altered. Insoluble organic matter does not appear to have acted as a source of carbon for carbonate formation (Alexander et al., 2007; Vacher et al., 2017). By contrast, SOM was progressively oxidized, lowering its H/C ratios (Isa et al., 2021) and reducing its abundance as carbon was repurposed in carbonate minerals. In addition, carbon-bearing ices donated carbon for carbonate precipitation (Alexander et al., 2015; Vacher et al., 2017; Telus et al., 2019).

In addition, to an inherited heavy carbon isotope composition, the observed heavy carbon could be the result of atmospheric heating by the preferential loss of ^{12}C from the labile materials. Organics interacting with water at high temperature show decomposition as well as reorganization of the organic molecules to form more complex aromatics from straight chain alkanes. This re-organization could also potentially lead to a release of ^{12}C. However, these processes would affect the exterior of the particle, and not the interior where the carbonate peaks were observed. In addition, the presence of F1_207 with ^{12}C enrichments survived the entry process. An evolution to a slightly heavier carbon isotope signature cannot be completely ruled out. Presumably this reflects changes in the composition of organics, with loss of light carbon as the carbonaceous material becomes more refractory.

Secondary carbonate minerals in carbonaceous chondrites have isotopically heavy compositions ($\delta^{13}C$: −7.4 to +79.7‰, Guo and Eiler, 2007; Alexander et al., 2015, Fig. 3), reflecting a combination of potential processes:

1. Carbonate compositions were partially controlled by the composition inherited from their precursor phases (ices and SOM). Thus, oxidation of SOM rich in ^{13}C could have produced ^{13}C-rich carbonates. Alexander et al. (2015) speculated that reaction of the organic carbon mixing with radiation-generated peroxide could produce the carbonate compositions measured in CI-CM-CR chondrites.
2. Isotopic fractionation processes will have also imparted an effect and because aqueous alteration operated at low temperatures (<150 °C [e.g., Guo and Eiler, 2007]) fractionation effects are predicted to have been large (e.g., Fig. 11 in Vacher et al., 2017).
3. In addition, if open system gas loss occurred by kinetic isotope fractionation mechanisms (before or during aqueous alteration) this would have led to the preferential loss of light ^{12}C resulting in a ^{13}C-

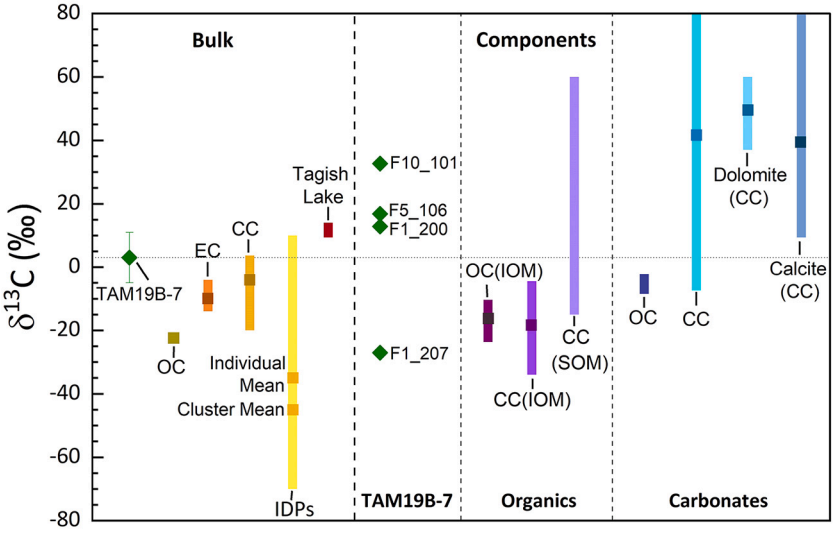

Fig. 5. $\delta^{13}C$ ‰ values of the solar system relative to VDPB. The TAM19B-7 bulk data in the first column of the plot is compared to bulk values from carbonaceous chondrites CCs (including Tagish Take), ordinary chondrites OCs, enstatite chondrites ECs and IDPs. The next column is subdivided to show the carbon anomalies in TAM19B-7 along with various components measured in meteorites including insoluble and soluble organic matter and carbonates (calcites and dolomite ranges shown separately). The IDP data included is from Messenger et al. (2003). Meteorite data is from Alexander et al. (2007, 2010, 2012, 2015) and Grady et al. (1988). The calcite and dolomite meteoritic data is from Tyra et al. (2016)); Vacher et al. (2017); and Telus et al. (2019). Domains in TAM19B-7 have $\delta^{13}C$ values comparable to that observed in Tagish Lake, bulk carbonates specifically calcites measured in CCs.

enriched signature in any later-formed carbonate minerals (Guo and Eiler, 2007; Alexander et al., 2015). Open system behavior could be achieved by a convecting hydrothermal system on a large body (Kaplan et al., 2020) or by near-surface gas escape on a small body with a high permeability (Guo and Eiler, 2007).

The heavy bulk composition of TAM19B-7 rules out isotopically light IOM as the principal carbon-bearing phase (despite the positive detection of aromatic-rich IOM from Raman spectral data (Fig. 5). Instead, this signature implies either SOM or carbonate minerals were the primary form of carbon in this micrometeorite. Carbonates as the dominant phases would be consistent with TAM19B-7's aqueously altered history (Suttle et al., 2019a), while SOM, which is destroyed during aqueous alteration (Isa et al., 2021) and decomposes during atmospheric entry (Suttle et al., 2019b) is unlikely to be responsible. Thus, the heavy bulk C-isotope composition of TAM19B-7 implies a carbonate dominated carbon budget.

Tagish Lake also has a carbonate-rich mineralogy (up to 15 vol.%, Blinova et al., 2014) containing calcite, dolomite, and Fe- and Mg-rich breunnerite spread through the matrix. These carbonates have consistently high $\delta^{13}C$ values (~70‰, Fujiya et al., 2019), being distinct from the carbonates in CM chondrites which generally have variable compositions and include lighter values (Alexander et al., 2015; Vacher et al., 2017). This led Fujiya et al. (2019) to conclude that the carbonates in Tagish Lake formed from ^{13}C-rich fluids whose heavy composition could only have been inherited from the heaviest precursor phase – ^{13}C-rich ices.

The heavy ^{13}C-rich hotspot values measured in TAM19B-7 have $\delta^{13}C$ values <35‰. These are distinct from Tagish Lake's carbonates (always >50‰). Consequently, although TAM19B-7 and Tagish Lake share similar bulk compositions their detailed C-isotope budgets were different. Instead, the heavy hotspots in TAM19B-7's are consistent with carbonates in CM/CR/CI chondrites. Calcites in the CM carbonaceous chondrites ALH 83100, ALH 84034 and MET 01070 show large isotopic variations ($\delta^{13}C$: from +10 to +80‰, Telus et al., 2019]), while dolomites have a more confined range and heavier compositions ($\delta^{13}C$: ~ + 40 to +60 ‰, Telus et al., 2019). Based on this comparison the positive $\delta^{13}C$ values in TAM19B-7 most likely suggest a calcite dominated mineralogy.

In summary, TAM19B-7's bulk composition is heavy (+3‰ ±8‰; 2σ). This ^{13}C-enrichment is unlikely to arise due to fractionation during atmospheric entry but rather occurred due to open system alteration or carbonate generation from isotopically heavy SOM. We rule out accretion of abundant ^{13}C-rich ices at large heliocentric formation distance because individual $\delta^{13}C$ hotspots do not have sufficiently heavy values.

5.4. ^{13}C anomalous domains

5.4.1. Light domain (F1–207)

F1–207 was the only anomalous measurement with a depleted $\delta^{13}C$ value of −27.1‰. Depletions in ^{13}C are commonly observed in extraterrestrial materials and associated with organic matter (Fig. 3) (Messenger et al., 2003). One main pathway for the formation of ^{13}C depletions are ion-molecule reactions in low-temperature interstellar clouds (Floss et al., 2004; Floss et al., 2010; Bose et al., 2012). Gas phase carbon in the C^+ family like H_2CO and CS favor fractionation leading to ^{12}C enhancement, especially in high density clouds, since $^{13}C^+$ is used more proportionally by CO (Langer et al., 1984; Tielens, 1998). There are multiple different carbon species present in these clouds, and the different species and reaction pathways fractionate differently. This ability to transfer carbon isotopes between different species is due to these two main reactions:

$$^{13}C^+ + {}^{12}CO \longleftrightarrow {}^{13}CO + {}^{12}C^+ \quad (1)$$

and

$$H^{12}CO^+ + {}^{13}CO \longleftrightarrow H^{13}CO^+ + {}^{12}CO \quad (2)$$

They enrich ^{13}C in CO and HCO^+ and deplete it in the other C species. This fractionation in the gas phase can be passed down to other species involved in grain surface chemistry that directly trace back to this gas-phase C. This process can lead to both enrichments and depletions in ^{13}C in carbonaceous materials, but these reactions happen on the individual grain-level and are unlikely to cause any effect on the bulk value. It is likely that this is the source of the depleted $\delta^{13}C$ value for F1_207, meaning F1–207 is interpreted as insoluble organic matter.

5.4.2. Heavy domains (F10_101, F5_106, and F1_200)

Three ^{13}C enriched hotspots were identified in TAM19B-7 (Fig. 2-3). Their compositions are consistent with carbonate minerals. F10_101 and F5_106, whose $\delta^{13}C$ values of 16.8‰ and 32.7‰ are enriched in ^{13}C, have $^{12}C^-/^{28}Si^-$ ratios of 0.9 and 1.5 respectively. Both the carbon isotopic composition and C/Si ratio can be indicative of presolar SiC grains (e.g., Floss et al., 2010; Bose et al., 2012, 2014), but the $\delta^{13}C$ anomalies of presolar SiC grains are typically >200‰, much higher than what is observed here, making it highly unlikely that our anomalies here are presolar grains. Additionally, TAM19B-7's petrology demonstrates advanced aqueous alteration which should lead to the destruction of presolar grains (Floss et al., 2010; Bose et al., 2014).

F1_200 has an enriched $\delta^{13}C$ value of 12.9‰ and an extremely high $^{12}C^-/^{28}Si^-$ ratio of 3.2×10^4, ruling out SiC grain as a possibility. The carbon-bearing phase for all three of these ^{13}C enrichments is likely carbonate grains. Carbonates, such as calcite, magnesite, siderite, and dolomite, have been identified in other fine-grained micrometeorites from Antarctica using techniques such as TEM, SEM, and XANES (Dobrică et al., 2009, 2019). So far, carbonates as small as 1.5 μm in an Antarctic micrometeorite has been identified (Dobrică et al., 2019). However, better resolution and the use of multiple laboratory techniques are required to confirm the existence of carbonates in TAM19B-7.

6. Implications

6.1. The parentage of TAM19B-7: Comparison with C-type asteroids

The 2.8 μm band in the near-IR reflectance spectra of TAM19B-7 (Fig. 2) indicates the presence of hydrated phases (i.e., phyllosilicates) and clearly links the particle to the C-type asteroid family. This feature is found on a wide variety of aqueously altered bodies including Ceres, Ryugu and Bennu (De Sanctis et al., 2015). Ceres' surface displays a variety of carbonates across its regolith (dolomite, magnesite, and calcite) and locally large abundances of sodium carbonate (Palomba et al., 2019). The species and associated minerals have been interpreted as evidence for aqueous alteration in a CO_2 rich environment (Castillo-Rogez et al., 2018).

Previous studies have shown that the band center position for phyllosilicates is sensitive to phyllosilicate cation content, shifting towards longer wavelength as the Fe content increases (Takir et al., 2013). This implies that TAM19B-7 has a higher Fe content than Ceres or Ryugu, which have a band centered at 2.7 μm. However, this band center shift might also be due to thermal effects (note that the spectra of TAM19B-7 was not acquired under asteroid-like conditions, but at room temperature).

TAM19B-7 also shares other similarities with C-type asteroids, notably absorption features located at 3.3–3.6 μm and 3.9 μm; these bands are related to organic matter and carbonates respectively. These phases are common on other minor bodies like Ryugu (Pilorget et al., 2022) and Themis (Rivkin and Emery, 2010). Organic matter is found on Ceres, in particular around the Ernutet crater where aliphatic hydrocarbons are found. However, whether the organic matter comes directly from the Solar Nebula or is generated by parent-body processes is still unknown. Likewise, carbonates are also detected on the surface of water

rich bodies (typically Mg or Ca-bearing for C-type asteroids; Na-bearing carbonates on Ceres) (De Sanctis et al., 2016; Kaplan et al., 2020; Simon et al., 2020). The Na_2CO_3 found in Occator is different from the Mg—Ca carbonate observed globally on Ceres, is generally not observed in carbonaceous chondrite meteorites. This could be a result of different and variable aqueous chemical processes on Ceres compared to other C-type asteroids or these phases are preferentially destroyed during sample handling and storage.

A direct link to a highly evolved body like Ceres is problematic, given that TAM19B-7 lacks the 3.1 μm band, associated with NH compounds, like the distinctive ammonium-bearing phyllosilicates found only on Ceres (De Sanctis et al., 2015). The 3.1 μm band has variable spectral profiles and subtly different band center positions (i.e., Ceres-like, Europa-like, rounded and sharp) (Usui et al., 2019). This band is difficult to detect among meteorites and micrometeorites; it has been found only in the CV3 Efremovka chondrite under asteroidal conditions (Takir et al., 2019). Generally, CCs have been found to be rich in ammonia (Pizzarello and Williams, 2012); this ammonia measured in acid-extracted insoluble organic matter is bonded directly to the organics. Additionally, the Fe-rich phyllosilicates found in TAM19B-7 are generally not expected to occur on Ceres because advanced aqueous alteration tends to remove Fe from phyllosilicates to form magnetite and FeS. Although the presence of anhydrous silicates in association with Fe-rich phyllosilicates in TAM19B-7 is an interesting observation, high phyllosilicate fraction and preservation of Fe-bearing phyllosilicates is an enigma.

6.2. *The survival of carbon during atmospheric entry*

Although carbon abundances in TAM19B-7 are low, the presence of D and G bands in Raman spectra and the presence of near-IR absorption bands over the wavelength range 3.3-3.9 μm are compelling evidence for the survival of C-bearing phases within this micrometeorite. This is despite significant thermal reprocessing (T < 800 °C C) during atmospheric entry. Organic matter suffered oxidation, graphitization and, in some cases complete thermal decomposition (as inferred from the absence of Raman D/G bands across most of the particle). Because organic matter in carbonaceous chondrites is often intimately mixed with phyllosilicate minerals (e.g., Piani et al., 2012) this association may have provided some protection from flash heating in TAM19B-7, and by inference in all fine-grained hydrated micrometeorites. The carbonate budget was likewise affected by heating. Both calcite and dolomite suffer complete decomposition at relatively moderate temperatures (T > 600 °C [Nozaki et al., 2006; Garenne et al., 2014; Haberle and Garvie, 2017; Karunadasa et al., 2019]), although decrepitation and the initial stages of degassing can occur at considerably lower temperatures (<400 °C [e.g. Rodriguez-Navarro et al., 2009]). Thus, former carbonates in TAM19B-7 are likely present as micron-scale partially decomposed mineraloids. Often overlooked due to their small size, the carbon in micrometeorites can survive flash heating and therefore can be a potential source of this biocritical element for early Earth.

7. Conclusions

Five fragments of micrometeorite TAM19B-7 were analyzed with the NanoSIMS to determine the carbon isotopic composition. The bulk $\delta^{13}C$ value of TAM19B-7 is +3 8‰. In addition, 4 anomalous domains with values of −27.1‰, +12.9‰, +16.8‰, and + 32.7‰ were identified. The bulk $\delta^{13}C$ composition of TAM19B-7 is heavier than most carbonaceous chondrites and most consistent with the compositions reported for Tagish Lake. Analysis of the ^{13}C enriched hotspots shows that the C-bearing phases in this micrometeorite were primarily calcites with compositions similar to those found in the CM chondrites. A carbonate dominated carbon budget, when paired with intensely aqueously altered C1 petrography and inferred ^{16}O-poor O-isotope composition, implies that TAM19B-7 originates from an ultra-hydrated, carbonaceous chondrite parent body that is likely not sampled by our meteorite record. Its ^{13}C-rich bulk composition is explained by carbonate formation driven primarily by the destruction of soluble organic matter, potentially with open system alteration further pushing fluid compositions to heavier values.

Declaration of Competing Interest

None.

Data availability

Raw data will be made available on request.

Acknowledgments

Special thanks to the funding provided by the Arizona Space Grant Consortium for Froh, startup funding for Bose from ASU, and the NanoSIMS assistance from Dr. Ziliang Jin. The collection and curation of the Antarctic micrometeorite investigated in this study was funded by the Italian Programma Nazionale delle Ricerche in Antartide (grant number PNRA16 00029). We thank Cristian Carli and Stefania Stefani for the access and support to the spectroscopy laboratory at the INAF Rome. We thank Dr. Matthew Genge and another anonymous reviewer for their comments that greatly improved the manuscript.

References

Akai, J., 1992. TTT diagram of serpentine and saponite, and estimation of metamorphic heating degree of Antarctic carbonaceous chondrites. Antarctic Meteorite Res. 5, 120–135.
Alexander, C.O.D., Fogel, M., Yabuta, H., Cody, G.D., 2007. The origin and evolution of chondrites recorded in the elemental and isotopic compositions of their macromolecular organic matter. Geochim. Cosmochim. Acta 71, 4380–4403.
Alexander, C.O.D., Newsome, S.D., Fogel, M.L., Nittler, L.R., Busemann, H., Cody, G.D., 2010. Deuterium enrichments in chondritic macromolecular material—implications for the origin and evolution of organics, water and asteroids. Geochim. Cosmochim. Acta 74, 4417–4437.
Alexander, C.O.D., Bowden, R., Fogel, M.L., Howard, K.T., Herd, C.D.K., Nittler, L.R., 2012. The provenances of asteroids, and their contributions to the volatile inventories of the terrestrial planets. Science 337, 721–723.
Alexander, C.O.D., Bowden, R., Fogel, M.L., Howard, K.T., 2015. Carbonate abundances and isotopic compositions in chondrites. Meteorit. Planet. Sci. 50, 810–833.
Aponte, J.C., McLain, H.L., Dworkin, J.P., Elsila, J.E., 2016. Aliphatic amines in Antarctic CR2, CM2, and CM1/2 carbonaceous chondrites. Geochim. Cosmochim. Acta 189, 296–311.
Battandier, M., Bonal, L., Quirico, E., Beck, P., Engrand, C., Duprat, J., Dartois, E., 2018. Characterization of the organic matter and hydration state of Antarctic micrometeorites: a reservoir distinct from carbonaceous chondrites. Icarus 306, 74–93.
Blinova, A.I., Zega, T.J., Herd, C.D., Stroud, R.M., 2014. Testing variations within the Tagish Lake meteorite—I: mineralogy and petrology of pristine samples. Meteorit. Planet. Sci. 49, 473–502.
Bose, M., Floss, C., Stadermann, F.J., Stroud, R.M., Speck, A.K., 2012. Circumstellar and interstellar material in the CO3 chondrite ALHA77307: an isotopic and elemental investigation. Geochim. Cosmochim. Acta 93, 77–101.
Bose, M., Zega, T.J., Williams, P., 2014. Assessment of alteration processes on circumstellar and interstellar grains in Queen Alexandra Range 97416. Earth Planet. Sci. Lett. 399, 128–138.
Busemann, H., Alexander, M.O.D., Nittler, L.R., 2007. Characterization of insoluble organic matter in primitive meteorites by microRaman spectroscopy. Meteorit. Planet. Sci. 42, 1387–1416.
Castillo-Rogez, Julie, Neveu, Marc, McSween, Harry Y., Fu, Roger R., Toplis, Michael J., Prettyman, Thomas, 2018. Insights into Ceres's evolution from surface composition. Meteorit. Planet. Sci. https://doi.org/10.1111/maps.13181.
Chan, Q.H., Nakato, A., Kebukawa, Y., Zolensky, M.E., Nakamura, T., Maisano, J.A., Colbert, M.W., Martinez, J.E., Kilcoyne, A.D., Suga, H., Takahashi, Y., 2019. Heating experiments of the Tagish Lake meteorite: investigation of the effects of short-term heating on chondritic organics. Meteorit. Planet. Sci. 54, 104–125.
Cordier, C., Folco, L., 2014. Oxygen isotopes in cosmic spherules and the composition of the near-earth interplanetary dust complex. Geochim. Cosmochim. Acta 146, 18–26.
Cordier, C., Baecker, B., Ott, U., Folco, L., Trieloff, M., 2018. A new type of oxidized and pre-irradiated micrometeorite. Geochim. Cosmochim. Acta 233, 135–158.
De Sanctis, M.C., Ammannito, E., Raponi, A., Marchi, S., McCord, T.B., McSween, H.Y., Capaccioni, F., Capria, M.T., Carrozzo, F.G., Ciarniello, M., Longobardo, A., 2015. Ammoniated phyllosilicates with a likely outer Solar System origin on (1) Ceres. Nature 528, 241–244.

De Sanctis, M.C., Raponi, A., Ammannito, E., Ciarniello, M., Toplis, M.J., McSween, H.Y., Castillo-Rogez, J.C., Ehlmann, B.L., Carrozzo, F.G., Marchi, S., Tosi, F., 2016. Bright carbonate deposits as evidence of aqueous alteration on (1) Ceres. Nature 536, 54–57.

Di Vincenzo, G., Folco, L., Suttle, M.D., Brase, L., Harvey, R.P., 2021. Multi-collector 40Ar/39Ar dating of microtektites from Transantarctic Mountains (Antarctica): a definitive link with the Australasian tektite/microtektite strewn field. Geochim. Cosmochim. Acta 298, 112–130.

Dionnet, Z., Suttle, M.D., Longobardo, A., Rotundi, A., Folco, L., Della Corte, V., King, A., 2020. X-ray computed tomography: morphological and porosity characterization of giant Antarctic micrometeorites. Meteorit. Planet. Sci. 55, 1581–1599.

Dobrică, E., Engrand, C., Duprat, J., Gounelle, M., Leroux, H., Quirico, E., Rouzaud, J.N., 2009. Connection between micrometeorites and Wild 2 particles: from Antarctic snow to cometary ice. Meteorit. Planet. Sci. 44, 1643–1661.

Dobrică, E., Ogliore, R.C., Engrand, C., Nagashima, K., Brearley, A.J., 2019. Mineralogy and oxygen isotope systematics of magnetite grains and a magnetite-dolomite assemblage in hydrated fine-grained Antarctic micrometeorites. Meteorit. Planet. Sci. 54, 1973–1989.

Dudorov, A.E., Eretnova, O.V., 2020. The rate of falls of meteorites and bolides. Sol. Syst. Res. 54, 223–235.

Engrand, C., Maurette, M., 1998. Carbonaceous micrometeorites from Antarctica. Meteorit. Planet. Sci. 33, 565–580.

Floss, Christine, Stadermann, Frank, 2009. Auger Nanoprobe analysis of presolar ferromagnesian silicate grains from primitive CR chondrites QUE 99177 and MET 00426. Geochim. Cosmochim. Acta 73 (8), 2415–2440. https://doi.org/10.1016/j.gca.2009.01.033.

Floss, C., Stadermann, F.J., Bradley, J., Bajt, S., Graham, G., 2004. Carbon and nitrogen isotopic anomalies in an anhydrous interplanetary dust particle. Science 303, 1355–1358.

Floss, C., Stadermann, F.J., Mertz, A.F., Bernatowicz, T.J., 2010. A NanoSIMS and Auger Nanoprobe investigation of an isotopically primitive interplanetary dust particle from the 55P/Tempel-Tuttle targeted stratospheric dust collector. Meteorit. Planet. Sci. 45, 1889–1905.

Folco, L., Cordier, C., 2015. Micrometeorites. EMU Notes Mineral. 15, 253–297.

Folco, L., D'Orazio, M., Tiepolo, M., Tonarini, S., Ottolini, L., Perchiazzi, N., Rochette, P., Glass, B.P., 2009. Transantarctic Mountain microtektites: geochemical affinity with Australasian microtektites. Geochim. Cosmochim. Acta 73, 3694–3722.

Fujiya, W., Hoppe, P., Ushikubo, T., Fukuda, K., Lindgren, P., Lee, M.R., Koike, M., Shirai, K., Sano, Y., 2019. Migration of D-type asteroids from the outer Solar System inferred from carbonate in meteorites. Nat. Astron. 3, 910–915.

Garenne, A., Beck, P., Montes-Hernandez, G., Chiriac, R., Toche, F., Quirico, E., Bonal, L., Schmitt, B., 2014. The abundance and stability of "water" in type 1 and 2 carbonaceous chondrites (CI, CM and CR). Geochim. Cosmochim. Acta 137, 93–112.

Genge, M.J., 2006. Igneous rims on micrometeorites. Geochim. Cosmochim. Acta 70, 2603–2621.

Genge, M.J., 2007. Micrometeorites and their implications for meteors. In: Advances in Meteoroid and Meteor Science, pp. 525–535.

Genge, M.J., 2008. Koronis asteroid dust within Antarctic ice. Geology 36, 687–690.

Genge, M.J., Grady, M.M., Hutchison, R., 1997. The textures and compositions of fine-grained Antarctic micrometeorites: implications for comparisons with meteorites. Geochim. Cosmochim. Acta 61, 5149–5162.

Genge, M.J., Engrand, C., Gounelle, M., Taylor, S., 2008. The classification of micrometeorites. Meteorit. Planet. Sci. 43, 497–515.

Genge, M.J., Suttle, M., Van Ginneken, M., 2017. Thermal shock fragmentation of mg silicates within scoriaceous micrometeorites reveal hydrated asteroidal sources. Geology 45, 891–894.

Gilmour, I., 2014. Structural and isotopic analysis of organic matter in carbonaceous chondrites. Treatise Geochem. 215–233.

Gonczi, R., Froeschlé, C., Froeschle, C., 1982. Poynting-Robertson drag and orbital resonance. Icarus 51, 633–654.

Gounelle, M., Chaussidon, M., Morbidelli, A., Barrat, J.A., Engrand, C., Zolensky, M.E., Mckeegan, K.D., 2009. A unique basaltic micrometeorite expands the inventory of solar system planetary crusts. Proc. Natl. Acad. Sci. 106, 6904–6909.

Grady, M.M., Wright, I.P., Swart, P.K., Pillinger, C.T., 1988. The carbon and oxygen isotopic composition of meteoritic carbonates. Geochim. Cosmochim. Acta 52, 2855–2866.

Gröning, Manfred, 2004. International stable isotope reference materials. In: Handbook of Stable Isotope Analytical Techniques. Elsevier, pp. 874–906.

Guo, W., Eiler, J.M., 2007. Temperatures of aqueous alteration and evidence for methane generation on the parent bodies of the CM chondrites. Geochim. Cosmochim. Acta 71, 5565–5575.

Haberle, C.W., Garvie, L.A., 2017. Extraterrestrial formation of oldhamite and portlandite through thermal metamorphism of calcite in the Sutter's Mill carbonaceous chondrite. Am. Mineral. 102, 2415–2421.

Hässig, M., Altwegg, K., Balsiger, H., Berthelier, J.J., Bieler, A., Calmonte, U., Dhooghe, F., Fiethe, B., Fuselier, S.A., Gasc, S., Gombosi, T.I., 2017. Isotopic composition of CO2 in the coma of 67P/Churyumov-Gerasimenko measured with ROSINA/DFMS. Astron. Astrophys. 605, A50.

Howard, K.T., Alexander, C.O.D., Schrader, D.L., Dyl, K.A., 2015. Classification of hydrous meteorites (CR, CM and C2 ungrouped) by phyllosilicate fraction: PSD-XRD modal mineralogy and planetesimal environments. Geochim. Cosmochim. Acta 149, 206–222.

Isa, J., Orthous-Daunay, F.R., Beck, P., Herd, C.D., Vuitton, V., Flandinet, L., 2021. Aqueous alteration on asteroids simplifies soluble organic matter mixtures. Astrophys. J. Lett. 920, L39.

Kaplan, H.H., Lauretta, D.S., Simon, A.A., Hamilton, V.E., DellaGiustina, D.N., Golish, D. R., Reuter, D.C., Bennett, C.A., Burke, K.N., Campins, H., Connolly, H.C., 2020. Bright carbonate veins on asteroid (101955) Bennu: implications for aqueous alteration history. Science 370, eabc3557.

Karunadasa, K.S., Manoratne, C.H., Pitawala, H.M.T.G.A., Rajapakse, R.M.G., 2019. Thermal decomposition of calcium carbonate (calcite polymorph) as examined by in-situ high-temperature X-ray powder diffraction. J. Phys. Chem. Solids 134, 21–28.

Kurat, G., Koeberl, C., Presper, T., Brandstätter, F., Maurette, M., 1994. Petrology and geochemistry of Antarctic micrometeorites. Geochim. Cosmochim. Acta 58, 3879–3904.

Langer, W.D., Graedel, T.E., Frerking, M.A., Armentrout, P.B., 1984. Carbon and oxygen isotope fractionation in dense molecular clouds. Astrophys. J. 277, 581–604.

Maurette, M., 1996. Carbonaceous micrometeorites and the origin of life. Orig. Life Evol. Biosph. 28, 385–412.

Messenger, S., Stadermann, F.J., Floss, C., Nittler, L.R., Mukhopadhyay, S., 2003. Isotopic signatures of presolar materials in interplanetary dust. Solar Syst. History Isotop. Sig. Volatile Elements 155–172.

Noguchi, T., Ohashi, N., Tsujimoto, S., Mitsunari, T., Bradley, J.P., Nakamura, T., Toh, S., Stephan, T., Iwata, N., Imae, N., 2015. Cometary dust in Antarctic ice and snow: past and present chondritic porous micrometeorites preserved on the Earth's surface. Earth Planet. Sci. Lett. 410, 1–11.

Nozaki, W., Nakamura, T., Noguchi, T., 2006. Bulk mineralogical changes of hydrous micrometeorites during heating in the upper atmosphere at temperatures below 1000 C. Meteorit. Planet. Sci. 41, 1095–1114.

Palomba, E., Longobardo, A., De Sanctis, M.C., Stein, N.T., Ehlmann, B., Galiano, A., Raponi, A., Ciarniello, M., Ammannito, E., Cloutis, E., Carrozzo, F.G., M.T.Capria, Stephan, K., Zambon, F., Tosi, F., Raymond, C.A., Russell, C.T., 2019. Compositional differences among Bright Spots on the Ceres surface. Icarus 320 (1), 202–212. https://doi.org/10.1016/j.icarus.2017.09.020.

Piani, L., Remusat, L., Robert, F., 2012. Determination of the H isotopic composition of individual components in fine-scale mixtures of organic matter and phyllosilicates with the nanoscale secondary ion mass spectrometry. Anal. Chem. 84, 10199–10206.

Pilorget, C., Okada, T., Hamm, V., Brunetto, R., Yada, T., Loizeau, D., Riu, L., Usui, T., Moussi-Soffys, A., Hatakeda, K., Nakato, A., Yogata, K., Abe, M., Aléon-Toppani, A., Carter, J., Chaigneau, M., Crane, B., Gondet, B., Kumagai, K., Langevin, Y., Lantz, C., Le Pivert-Jolivet, T., Lequertier, G., Lourit, L., Bibring, J.-P., 2022. First compositional analysis of Ryugu samples by the MicrOmega hyperspectral microscope. Nature Astronomy 6, 221–225.

Pizzarello, S., Williams, L.B., 2012. Ammonia in the early solar system: an account from carbonaceous meteorites. Astrophys. J. 749, 161.

Rivkin, A.S., Emery, J.P., 2010. Detection of ice and organics on an asteroidal surface. Nature 464, 1322–1323.

Rochette, P., Folco, L., Suavet, C., Van Ginneken, M., Gattacceca, J., Perchiazzi, N., Braucher, R., Harvey, R.P., 2008. Micrometeorites from the transantarctic mountains. Proc. Natl. Acad. Sci. 105, 18206–18211.

Rodriguez-Navarro, C., Ruiz-Agudo, E., Luque, A., Rodriguez-Navarro, A.B., Ortega-Huertas, M., 2009. Thermal decomposition of calcite: mechanisms of formation and textural evolution of CaO nanocrystals. Am. Mineral. 94, 578–593.

Rudraswami, N.G., Genge, M.J., Marrocchi, Y., Villeneuve, J., Taylor, S., 2020. The oxygen isotope compositions of large numbers of small cosmic spherules: implications for their sources and the isotopic composition of the upper atmosphere. J. Geophys. Res. Planets 125 p.e2020JE006414.

Sephton, M.A., 2002. Organic compounds in carbonaceous meteorites. Geochim. Cosmochim. Acta 71, 2361–2382.

Simon, A.A., Kaplan, H.H., Hamilton, V.E., Lauretta, D.S., Campins, H., Emery, J.P., Barucci, M.A., DellaGiustina, D.N., Reuter, D.C., Sandford, S.A., Golish, D.R., 2020. Widespread carbon-bearing materials on near-Earth asteroid (101955) Bennu. Science 370, eabc3522.

Soens, B., Chernonozhkin, S.M., de Vega, C.G., Vanhaecke, F., van Ginneken, M., Claeys, P., Goderis, S., 2022. Characterization of achondritic cosmic spherules from the Widerøefjellet micrometeorite collection (Sør Rondane Mountains, East Antarctica). Geochim. Cosmochim. Acta 325, 106–128.

Suavet, C., Rochette, P., Kars, M., Gattacceca, J., Folco, L., Harvey, R.P., 2009. Statistical properties of the Transantarctic Mountains (TAM) micrometeorite collection. Polar Sci. 3, 100–109.

Suavet, C., Alexandre, A., Franchi, I.A., Gattacceca, J., Sonzogni, C., Greenwood, R.C., Folco, L., Rochette, P., 2010. Identification of the parent bodies of micrometeorites with high-precision oxygen isotope ratios. Earth Planet. Sci. Lett. 293, 313–320.

Suavet, C., Gattacceca, J., Rochette, P., Folco, L., 2011. Constraining the terrestrial age of micrometeorites using their record of the Earth's magnetic field polarity. Geology 39, 123–126.

Suttle, M.D., Folco, L., 2020. The extraterrestrial dust flux: size distribution and mass contribution estimates inferred from the Transantarctic Mountains (TAM) micrometeorite collection. J. Geophys. Res. Planets 125 e2019JE006241.

Suttle, M.D., Genge, M.J., Folco, L., Russell, S.S., 2017. The thermal decomposition of fine-grained micrometeorites, observations from mid-IR spectroscopy. Geochim. Cosmochim. Acta 206, 112–136.

Suttle, M.D., Folco, L., Genge, M.J., Russell, S.S., Najorka, J., van Ginneken, M., 2019a. Intense aqueous alteration on C-type asteroids: perspectives from giant fine-grained micrometeorites. Geochim. Cosmochim. Acta 245, 352–373.

Suttle, M.D., Genge, M.J., Folco, L., Van Ginneken, M., Lin, Q., Russell, S.S., Najorka, J., 2019b. The atmospheric entry of fine-grained micrometeorites: the role of volatile gases in heating and fragmentation. Meteorit. Planet. Sci. 54, 503–520.

Suttle, M.D., Dionnet, Z., Franchi, I., Folco, L., Gibson, J., Greenwood, R.C., Rotundi, A., King, A., Russell, S.S., 2020. Isotopic and textural analysis of giant unmelted

micrometeorites–identification of new material from intensely altered 16O-poor water-rich asteroids. Earth Planet. Sci. Lett. 546, 116444.
Takir, D., Emery, J.P., Mcsween Jr., H.Y., Hibbitts, C.A., Clark, R.N., Pearson, N., Wang, A., 2013. Nature and degree of aqueous alteration in CM and CI carbonaceous chondrites. Meteorit. Planet. Sci. 48, 1618–1637.
Takir, D., Stockstill-Cahill, K.R., Hibbitts, C.A., Nakauchi, Y., 2019. 3-μm reflectance spectroscopy of carbonaceous chondrites under asteroid-like conditions. Icarus 333, 243–251.
Taylor, S., Lever, J.H., Harvey, R.P., 1998. Accretion rate of cosmic spherules measured at the South Pole. Nature 392, 899–903.
Taylor, S., Matrajt, G., Guan, Y., 2012. Fine-grained precursors dominate the micrometeorite flux. Meteorit. Planet. Sci. 47, 550–564.
Teichert, Z., Bose, M., Williams, P., Hervig, R., Williams, L., 2022. SIMS standards for lithium in carbonaceous matrices. Geostand. Geoanalytic. Res. https://doi.org/10.17632/92tgdmn45y.1.
Telus, M., Hauri, E.H., Wang, J., 2019. Calcite and dolomite formation in the CM parent body: insight from in situ C and O isotope analyses. Geochim. Cosmochim. Acta 260, 275–291.
Tielens, A.G.G.M., 1998. Deuterium and interstellar chemical processes. In: Bernatowicz, T., Zinner, E. (Eds.), Astrophysical Implications of the Laboratory Study of Presolar Materials. American Institute of Physics, pp. 523–544.
Toppani, A., Libourel, G., Engrand, C., Maurette, M., 2001. Experimental simulation of atmospheric entry of micrometeorites. Meteorit. Planet. Sci. 36, 1377–1396.
Tyra, Mark, Brearley, Adrian, Guan, Yunbin, 2016. Episodic carbonate precipitation in the CM chondrite ALH 84049: An ion microprobe analysis of O and C isotopes. Geochim. Cosmochim. Acta 175, 195–207. https://doi.org/10.1016/j.gca.2015.10.034.
Usui, F., Hasegawa, S., Ootsubo, T., Onaka, T., 2019. AKARI/IRC near-infrared asteroid spectroscopic survey: AcuA-spec. In: Publications of the Astronomical Society of Japan, 71, p. 1.
Vacher, L.G., Marrocchi, Y., Villeneuve, J., Verdier-Paoletti, M.J., Gounelle, M., 2017. Petrographic and C & O isotopic characteristics of the earliest stages of aqueous alteration of CM chondrites. Geochim. Cosmochim. Acta 213, 271–290.
Van Ginneken, M., Folco, L., Cordier, C., Rochette, P., 2012. Chondritic micrometeorites from the Transantarctic Mountains. Meteorit. Planet. Sci. 47, 228–247.
Van Ginneken, M., Genge, M.J., Folco, L., Harvey, R.P., 2016. The weathering of micrometeorites from the Transantarctic Mountains. Geochim. Cosmochim. Acta 179, 1–31.
Van Ginneken, M., Gattacceca, J., Rochette, P., Sonzogni, C., Alexandre, A., Vidal, V., Genge, M.J., 2017. The parent body controls on cosmic spherule texture: evidence from the oxygen isotopic compositions of large micrometeorites. Geochim. Cosmochim. Acta 212, 196–210.
Zook, H.A., Berg, O.E., 1975. A source for hyperbolic cosmic dust particles. Planet. Space Sci. 23, 183–203.